


Spin-momentum-locking-induced dynamic circular dichroism in extraordinary optical transmission

P. Moroshkin ^{1,*}, M.-J. Yu,¹ and J. Xu^{1,2}

¹*School of Engineering, Brown University, Providence, Rhode Island 02912, USA*

²*Department of Physics, Brown University, Providence, Rhode Island 02912, USA*



(Received 5 November 2022; accepted 10 March 2023; published 16 March 2023)

We present an experimental and theoretical study of circular dichroism observed in a symmetric nanohole array in a metal film—a nonchiral planar structure exhibiting extraordinary optical transmission. The effect is attributed to an extrinsic chirality dynamically induced in the excitation of surface plasmon polariton waves via spin-momentum locking.

DOI: [10.1103/PhysRevA.107.033504](https://doi.org/10.1103/PhysRevA.107.033504)

I. INTRODUCTION

Chirality is a fundamental degree of freedom which has been deployed in nature and in physical systems to remarkable effects. Enantiomers, mirror-pairs of molecules of opposite chirality, are good examples. They are identical in atomic composition and thus indistinguishable in scalar physical properties, but have starkly different effects in living systems: one can be toxic and cancer causing, the other therapeutic [1]. In sciences, it has played critical roles in analytical chemistry, crystallography, and material sciences. In engineering practices, one may also cite gyroscopes as one of its more recent and prominent applications. Artificial chiral materials are being developed and explored for meeting the everlasting demand for better, cheaper, and more compact technologies. While most of these newer developments have focused on constructing three-dimensional (3D) metamolecules, it is known that two-dimensional (2D) plasmonic chiral structures, in particular nanohole arrays, could also exhibit various chiroptic effects, in particular circular dichroism [2,3]. In such cases, the chirality is typically achieved by fabricating chiral-shaped nanoholes [4,5] or slits, or by the arrangement of several nanoholes into a unit cell that possesses chirality (handedness) [6,7]. Circular dichroism was also demonstrated in planar metasurfaces whose unit cell is nonchiral [8–10] but also noncentrosymmetric. In such a system it is then possible to align the system to a direction of the incident light to induce an extrinsic chirality [8].

Even more counterintuitive is the presence of circular dichroism found in a symmetric square array of circular nanoholes, as reported in Refs. [11–13]. Such structure clearly has an inversion symmetry. The experiments and numeric computations [11,13] revealed that the effect originates from the interference of propagating surface plasmon polariton (SPP) waves. The chiral response is observed under an oblique incidence of light, with the symmetry axes of the array rotated away from the plane of incidence.

Here we report on dynamic circular dichroism measured in a symmetric square array of circular nanoholes and offer evidence of spin-momentum locking (SML) in its explanation. The experiments are conducted in the transmission mode, which also exhibits the extraordinary optical transmission (EOT) effect as designed. Since the EOT effect is well established [14], the focus of this study is placed on the dichroism that is dynamically induced in the transmission of circularly polarized light.

The circularly polarized light induces a unidirectional surface plasmon polariton wave when their spin momenta match (lock) [15–17]. Thus, the vector components of the SPP waves excited by the left and right circularly polarized lights under otherwise identical conditions propagate in opposite directions, a phenomenon referred to as quantum spin Hall effect of light in Ref. [18]. Experimentally, this was observed via the emission produced by SPP scattering on defects [16,19–21], by near-field scanning optical microscopy [6], and by measuring the SPP-induced photocurrent (optical rectification) [22]. Locking of the spin degree of freedom and the propagation directions of electromagnetic waves (linear momentum) was also observed in more complex 2D nano structures and metasurfaces [23,24] and in optical fibers [25].

In the experiments with symmetric nanohole arrays [11–13], as well as in the present work, the handedness that is missing structurally in the sample is thus provided by the spin-momentum locking of the incident light to the corresponding SPP mode. As such, the spin-momentum-locking view complements the numerical simulations with the benefits of more physical and more general insights and guidance for designs and applications. Although the propagation directions of the SPP waves excited by left or right circularly polarized light are different, in the transmission and reflection spectra the corresponding SPP resonances may appear at the same wavelength and incidence angle and thus remain indistinguishable in the intensity spectrum. This degeneracy is lifted when the incidence plane is tilted relative to the sample plane, or rotated relative to the symmetry axes of the square array. By rotating the symmetry axes of the 2D array away from the plane of incidence and thereby effecting a symmetry-breaking action,

*petr_moroshkin@brown.edu

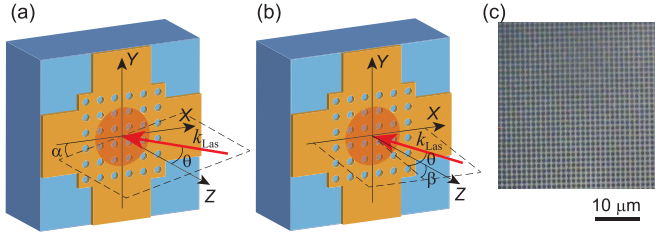


FIG. 1. (a) and (b) Illustrations showing the 2D plasmonic nanohole array used in the experiment and the incident laser beam (red arrow). The plane of incidence is shown by dashed lines. The symmetry is broken (a) by rotation of the incidence plane around the z axis and (b) by tilt of the incidence plane around the x axis. (c) Microscope image of the nanohole array.

a dynamic circular dichroism is observed in the experiments as described below.

II. EXPERIMENT

A. Experimental setup

Our experimental configuration is shown in Fig. 1. Optical transmission is measured in a 150-nm-thick gold film on a glass substrate, with a 3-nm-thick Cr adhesion layer. The film is patterned with a periodic square array of nanoholes perforating through the metal. The holes have a nominal diameter of 600 nm and a period $D = 1200$ nm in both the x and y directions. A microscope image of the array is shown in Fig. 1(c). It was fabricated by means of electron-beam lithography and a wet-etching process.

The nanohole array has an area of $300 \times 300 \mu\text{m}$ and is placed in the center of a cross-shaped structure with electric contacts at all four ends. (The contacts are meant for future uses of a dc electric current associated with photon drag effect, and were not involved in this study.). The sample is mounted on a computer-controlled automated xy translation stage moving with a resolution of $0.1 \mu\text{m}$ over the distances of several millimeters.

The sample is illuminated by a cw solid state laser with the wavelength $\lambda_{\text{Las}} = 1064$ nm and a maximum power of 200 mW. The polarization state of the laser is prepared using the appropriate half-wave and quarter-wave plates. The laser beam is focused to a spot diameter (FWHM) of $50\text{--}100 \mu\text{m}$ and is incident on the sample at an angle θ . In the present experiment, the angle of incidence θ was varied in the range from -56° to $+56^\circ$.

As shown in Fig. 1, the plane of incidence is defined with respect to the xz plane of the sample. More precisely, the circular dichroism effect discussed below is observed when a small angle is introduced between the xz plane and the plane of incidence. We study two configurations illustrated in Figs. 1(a) and 1(b), respectively: a rotation of the incidence plane by an angle α around the sample normal (z axis) and a tilt of the incidence plane by an angle β around the x axis. The tilt angle β could be measured with an uncertainty of about 0.2° . The rotation angle α was measured with a much higher accuracy—about 0.01° . The latter measurement was made by translating the sample in the xy plane in $10\text{-}\mu\text{m}$ steps

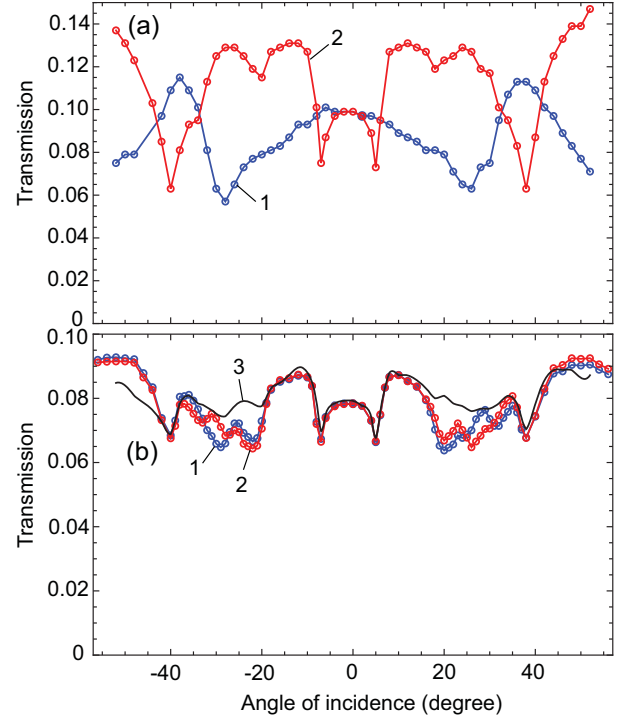


FIG. 2. Optical transmittance of the nanohole array. (a) Linearly polarized light. Curve 1 (blue) is vertical (S) polarization and curve 2 (red) is horizontal (P) polarization. (b) Circularly polarized light. Curve 1 (blue) is RCP, curve 2 (red) is LCP, and curve 3 (black) is $[T(S, \theta) + T(P, \theta)]/2$. Incidence in the xz (horizontal) plane.

and recording a 2D image (shadow) of the horizontal arms of the cross-shaped sample.

We record the power of the laser beam transmitted through the sample along the optical axis, i.e., the $(0,0)$ diffraction order in transmission.

B. Transmission measurements

According to the classical diffraction theory, the transmission through a subwavelength aperture of a radius a scales as $(a/\lambda_{\text{Las}})^4$. In the present experiments this dimensionless classical transmission reaches 6.3×10^{-3} . However, as discovered in Ref. [26], the excitation of SPP modes in the material surrounding the nanohole may lead to extraordinary optical transmission (EOT) [14]. In that case, the transmission normalized to the aperture area may exceed 100%.

Figure 2 shows the plots of the measured transmission through the nanohole array vs the angle of incidence for the 1064 nm laser. The transmission $T(\theta)$ varies between 0.06 and 0.14. In our sample, the total area of the nanoholes S_h covers 19.6% of the sample area S_{tot} . The normalized transmission $T(\theta)S_{\text{tot}}/S_h$ thus reaches 0.71, demonstrating the EOT effect.

We first discuss the transmission of lights of linear polarizations P and S , plotted in Fig. 2(a). For the P polarization, the transmission curve $T(P, \theta)$ has three pairs of symmetric (with respect to $\theta = 0$) absorptive resonances at $\theta = \pm 6^\circ, \pm 19^\circ$, and $\pm 39^\circ$. For the S polarization, we obtain $T(S, \theta)$ curve with a pair of broad dips at $\theta = \pm 27^\circ$ and a pair of maxima at $\theta = \pm 37^\circ$. Both the peaks and the dips

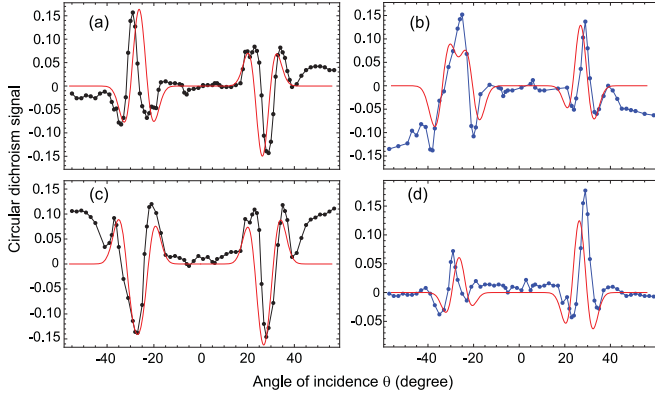


FIG. 3. Circular dichroism signals $G(\theta) = [T(L, \theta) - T(R, \theta)]/T(P, \theta = 0)$. Dots: Experimental data. Solid red line: Theoretical model. The incidence plain is rotated and tilted by (a) $\alpha = +0.24^\circ$, $\beta = -1.3^\circ$; (b) $\alpha = +4.5^\circ$, $\beta = -1.3^\circ$; (c) $\alpha = +1.3^\circ$, $\beta = +0.25^\circ$; and (d) $\alpha = -4.44^\circ$, $\beta = +0.25^\circ$.

in $T(S, \theta)$ are much broader than the resonances seen under the P polarized illumination. The observed spectral structure is attributed to the excitation of various SPP modes of the nanohole array, as discussed below in Sec. III A.

Now we turn to circularly polarized incidence and transmission. The measured transmission curves $T(L, \theta)$ and $T(R, \theta)$ corresponding to the left and right circularly polarized laser lights, respectively, are shown in Fig. 2(b). Assuming a linear light-matter interaction, one can represent both the right and left circularly polarized (RCP and LCP, respectively) lights as superpositions of two linearly polarized S and P components and thus expect for RCP and LCP two identical transmission profiles:

$$T(R, \theta) = T(L, \theta) = \frac{T(S, \theta) + T(P, \theta)}{2}. \quad (1)$$

The expected transmission profile is obtained with the help of Eq. (1), using the experimental $T(S, \theta)$ and $T(P, \theta)$ curves of Fig. 2(a), and is plotted in Fig. 2(b) as a solid black line.

The expected and measured transmission spectra agree very well for $|\theta| < 20^\circ$ and $|\theta| > 36^\circ$. However, a notable discrepancy is observed in the two symmetric ranges of the angle of incidence, $20^\circ < |\theta| < 36^\circ$. Note also the difference between the circularly polarized transmissions of $T(R, \theta)$ and $T(L, \theta)$ in this range [also Fig. 2(b)].

We obtain a circular dichroism signal $G(\theta)$ by taking the difference between the two circularly polarized transmission curves $T(L, \theta)$ and $T(R, \theta)$ and normalizing it to the transmission at normal incidence $T(P, \theta = 0) = T(S, \theta = 0) = 0.1$,

$$G(\theta) = \frac{T(L, \theta) - T(R, \theta)}{T(P, 0)}. \quad (2)$$

In Fig. 3 we plot four representative $G(\theta)$ curves obtained with the incidence plane slightly tilted and rotated with respect to the xz plane of the sample, as illustrated in Fig. 1.

III. THEORETICAL MODEL

A. SPP resonances of a square nanohole array

An SPP wave is excited when the momentum conservation condition is fulfilled. For the laser beam incident in the xz plane and a square nanohole array oriented along the x and y axes, one can write

$$\sqrt{(k_{\text{Las}} \sin \theta + nQ)^2 + (mQ)^2} = K_{\text{SPP}}(\omega_{\text{Las}}) \quad (3)$$

Here, $k_{\text{Las}} = 2\pi/\lambda_{\text{Las}}$ is the laser wave vector, θ is the angle of incidence, $Q = 2\pi/D$ is the lattice wave vector, and $K_{\text{SPP}}(\omega_{\text{Las}})$ is the in-plane wave vector of the SPP corresponding to the laser frequency. Assuming the excitation frequency is far detuned from the plasma frequency of the metal,

$$K_{\text{SPP}}(\omega_{\text{Las}}) = \frac{\omega_{\text{Las}}}{c} \sqrt{\frac{\varepsilon_1 \varepsilon_{\text{gold}}}{\varepsilon_1 + \varepsilon_{\text{gold}}}} \approx k_{\text{Las}} n_1, \quad (4)$$

where $\varepsilon_{\text{gold}}$ is the real part of the complex dielectric susceptibility of gold at the laser frequency and $n_1 = \sqrt{\varepsilon_1}$ is the refractive index of the medium adjacent to the gold film. $n_1 = 1$ for the SPP waves propagating at the gold-air interface and $n_1 = n_{\text{glass}}$ for the SPPs at the interface with the glass substrate. Here, n and m are integer indices characterizing the diffraction orders in the xz and yz plane, respectively.

Equations (3) and (4) are fulfilled when the corresponding diffracted mode propagates parallel to the surface, either at the air-gold or at the glass-gold interface. This defines a set of incidence angles $\theta_{n,m}$ at which various SPP modes are resonantly excited, leading to the increased absorption and dips in the transmission profile. The effect is known as Wood-Raleigh anomaly. We denote the resonances associated with the diffraction orders (n, m) in reflection and in transmission as $(n, m)^R$ and $(n, m)^T$, respectively. Below, in Fig. 4 all the resonance $\theta_{n,m}$ are marked out within our experimental range. It allows us to find the corresponding SPP resonances in the numerically calculated transmission profiles and identify those resonances observed experimentally.

B. Numeric model of light diffraction by the nanohole array

The transmission spectra and the diffraction of light on the nanohole array are modeled with the help of the COMSOL MULTIPHYSICS package. The model is built using a 3D geometry, including the gold film, on top of the glass substrate and the adhesion layer, with the space above the film being air. All material parameters and the geometry of the unit cell correspond to those of the sample in the experiment. Periodic boundary conditions are applied in both x and y directions, thus assuming that the nanohole array is infinite, as well as the laser beam cross section. The incident laser radiation is introduced via the periodic port at the upper boundary. The model provides relative intensities of all diffraction orders reflected and transmitted through the film.

Figure 4 shows the computed transmission through the nanohole array at the laser wavelength of 1064 nm, as a function of the angle of incidence. More precisely, we plot the intensity of the (0,0) diffraction order, normalized to the incident laser power. The same quantity is measured in the experiment.

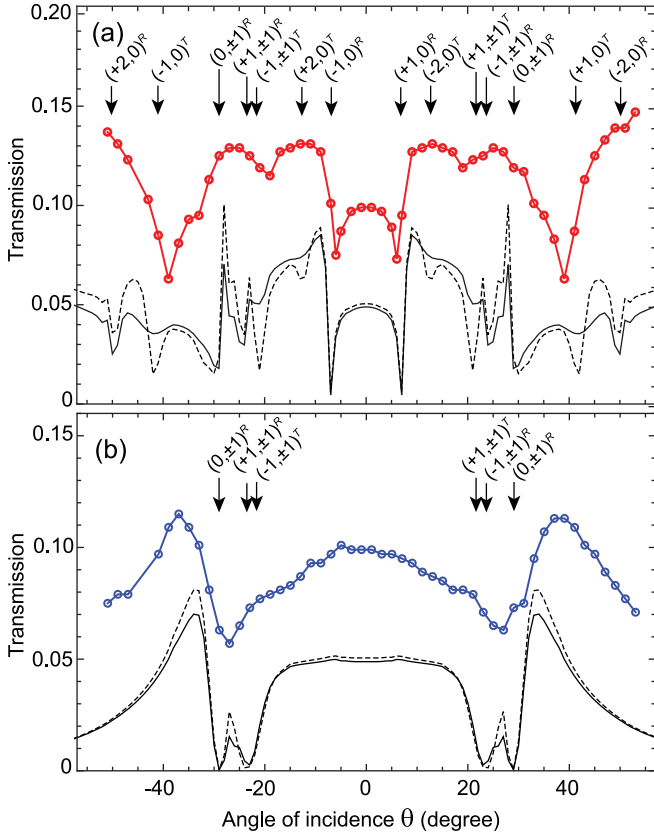


FIG. 4. Calculated transmission of the gold film with a nanohole array vs the angle of incidence. (a) P -polarized light; (b) S -polarized light. $\lambda_{\text{Las}} = 1064$ nm. Dashed black lines: COMSOL model without the adhesion layer. Solid black lines: COMSOL model with Cr adhesion layer. red (blue) line and dots: Experimental data (same as in Fig. 2). Vertical arrows indicate SPP resonances according to Eq. (3).

Two curves shown in Fig. 4(a) represent the transmission for the P -polarized light. The dashed curve is obtained assuming no adhesion layer of Cr between the gold film and the glass. The solid curve is generated with the model including the Cr layer, as in the experimental sample. This allows us to highlight the structures (dips and peaks) resulting from the coupling of the incident light with the SPP modes localized at the interface between the metal film and the substrate. In the presence of a thin Cr layer, these SPP modes become broadened and reduced in amplitude due to a stronger damping of SPP in Cr compared to Au.

The SPP resonance angles $\theta_{n,m}$ obtained by solving Eqs. (3) and (4) are marked with vertical arrows. Each resonance results in a dip in the computed transmission curve. For comparison, in the same figure we plot the experimentally measured transmission data of Fig. 2(a). The three pairs of absorptive peaks in the experimental curve can be identified with the SPP modes: $(\pm 1, 0)^T$ at $\theta = \pm 39^\circ$, $(\pm 1, \pm 1)^T$ at $\theta = \pm 20^\circ$, and $(\pm 1, 0)^R$ at $\theta = \pm 6^\circ$. $(\pm 1, 0)^T$ and $(\pm 1, \pm 1)^T$ are localized at the back surface and $(\pm 1, 0)^R$ at the front surface. Interestingly, the experimentally observed transmission significantly exceeds the computed data, including at the features corresponding to the EOT effect [26]. This could be attributed to a systemic deviation between the computational

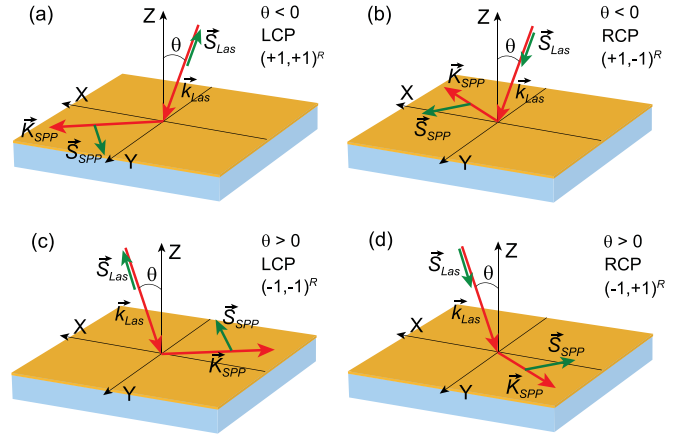


FIG. 5. An illustration showing the correspondence between the directions of K_{SPP} , S_{SPP} , and S_{Las} .

model of the material and structural parameters and the actual sample.

In Fig. 4(b) we plot the calculated and measured transmission data for the S -polarized laser. Here, the calculations with and without the Cr layer produce very similar results, suggesting that the light mostly couples to the front surface. The overall shape of the experimental curve is reproduced quite well, although in the experimental data both the peaks and the dips are significantly broadened. The broad dips at $\theta = \pm 27^\circ$ probably result from closely lying and overlapping two groups of SPP modes: $(\pm 1, \pm 1)^R$ at $\theta = \pm 24^\circ$ and $(0, \pm 1)^R$ at $\theta = \pm 29^\circ$.

C. Unidirectional SPP excitation

An important feature of the coupling between SPP waves and circularly polarized incident laser light results from the effect of spin-momentum locking [19,22]. The latter stems from the fact that a linearly polarized evanescent wave, such as an SPP, possesses a transversal spin momentum, directed orthogonally to its propagation direction [15,16].

$$S_{\text{SPP}} = \frac{[\text{Re}(k_{\text{SPP}})\text{Im}(k_{\text{SPP}})]}{[\text{Re}(k_{\text{SPP}})]^2}. \quad (5)$$

Given the evanescent nature of the SPP wave, k_{SPP} is a complex SPP wave vector. Its real part determining the propagation direction lies in the plane of the metal surface and is denoted K_{SPP} above. The imaginary part of k_{SPP} is directed orthogonal to the surface and describes the exponential decay of the SPP field in the space above.

It was recently demonstrated [19,21,22] that a circularly polarized laser light with its spin S_{Las} directed either parallel or antiparallel to its wave vector predominantly excites the SPP wave with S_{SPP} pointing in the same direction as S_{Las} , i.e., spin-momentum locking. For the geometry of our experiment, the effect is sketched in Fig. 5. Each of the SPP resonances $(n, m)^R$ or $(n, m)^T$ with $m \neq 0$ (i.e., diffraction in yz plane) is doubly degenerate. There are two SPP modes propagating along the same interface, symmetrically with respect to the x axis, with the wave vectors $K_{\text{SPP1}} = (K_x, mQ, 0)$ and $K_{\text{SPP2}} = (K_x, -mQ, 0)$, that can be excited at the same angle of incidence θ . However, at $\theta > 0$, the spin-momentum lock-

ing allows the RCP wave to excite only the SPP propagating in the positive y direction, along K_{SPP1} , whereas the LCP wave is able to excite only the SPP along K_{SPP2} . At $\theta < 0$, the coupling is switched to the opposite: RCP excites the SPP modes propagating in the negative y direction (K_{SPP2}) and LCP excites K_{SPP1} .

The unidirectional SPP excitation by a circularly polarized laser light is expected to manifest itself in the optical rectification effect by inducing a photocurrent in a transversal direction with respect to the plane of incidence. The effect was observed [27] in a 2D nanohole array very similar to that studied by us and more recently in a one-dimensional (1D) diffraction grating [22]. However, due to the degeneracy of the resonant SPP excitation angles, $\theta_{n,m} = \theta_{n,-m}$, one expects no difference between the transmission profiles obtained with RCP and LCP light in the present experimental configuration. Nevertheless, such difference is observed and is attributed to the deviation of the laser plane of incidence from the xy plane of the sample. Below, we demonstrate that a nonzero y component of the incident light wave vector that can be obtained either by tilt or by rotation of the sample leads to a pronounced circular dichroism effect in the transmission angular spectrum.

D. SPP resonances under tilt and rotation

In order to lift the degeneracy of the SPP resonances excited by RCP and LCP incident light, we consider two types of transformations: rotating the incidence plane by a small angle α around the z axis of the sample and tilting the incidence plane by another small angle β about the x axis. The former leads to a nonzero y component of the incident light (and SPP) wave vector given by

$$\begin{aligned} k_x &= k_{\text{Las}} \sin \theta \cos \alpha \\ k_y &= k_{\text{Las}} \sin \theta \sin \alpha. \end{aligned} \quad (6)$$

The latter leads to

$$\begin{aligned} k_x &= k_{\text{Las}} \sin \theta \\ k_y &= k_{\text{Las}} \cos \theta \sin \beta. \end{aligned} \quad (7)$$

The SPP momentum conservation Eq. (3) is then modified:

$$\sqrt{(k_x + nQ)^2 + (k_y + mQ)^2} = K_{\text{SPP}}(\omega_{\text{Las}}) \approx k_{\text{Las}} n_1. \quad (8)$$

We can then solve Eq. (8) to find the resonant incidence angle $\theta_{n,m}$ for each SPP resonance in a tilted or rotated sample.

In Fig. 6 we plot the calculated values of $\theta_{n,m}$ as functions of α and β , respectively. As expected, the degeneracy of each resonance with $m \neq 0$ is lifted. The closely lying $(0, \pm 1)^R$ and $(\pm 1, \pm 1)^R$ resonances start to overlap and cross each other already at $\alpha \approx 2.8^\circ$, or at $\beta \approx 1.4^\circ$. This results in a complex transmission profile, as a function of θ .

The experimental transmission resonances observed in the present work at $\lambda_{\text{Las}} = 1064$ nm have a typical angular width of $\sim 6^\circ$. We represent each of the $(0, \pm 1)^R$ and $(\pm 1, \pm 1)^R$ resonances with a Gaussian curve with a center corresponding to the resonance angle $\theta_{n,m}$ and a FWHM $w_0 = 6^\circ$. We then obtain the circular dichroism signal $G(\theta) = [T(L, \theta) -$

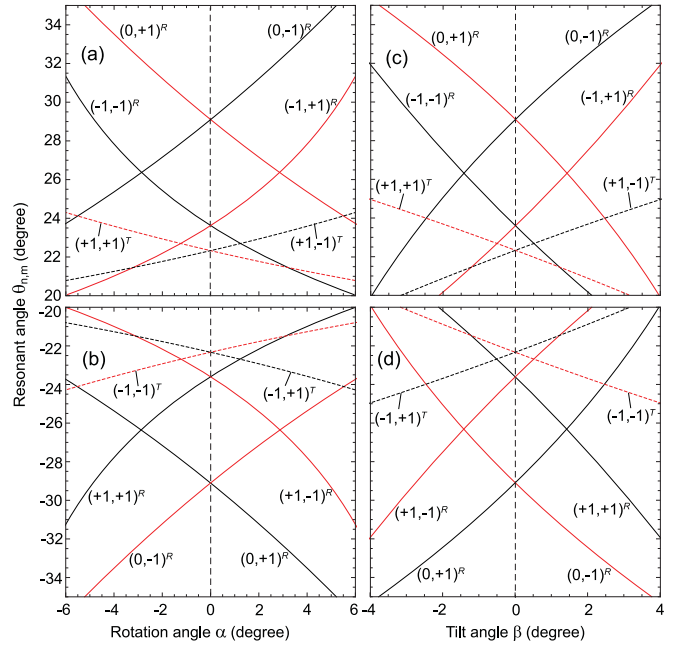


FIG. 6. (a) and (b) Calculated resonance angle $\theta_{n,m}$ vs the rotation angle α . (c) and (d) $\theta_{n,m}$ vs tilt angle β . Solid lines: SPP modes at the metal-air interface. Dashed lines: SPP modes at the metal-glass interface. Modes coupled to LCP light are shown in black, coupled to RCP in red.

$T(R, \theta)]/T_0$. The results are plotted in Fig. 3, together with the experimental data sets processed in the same way.

Introducing a nonzero rotation angle α (assuming $\beta = 0$) leads to a pair of bipolar features in the $G(\theta)$ profile, symmetric with respect to $\theta = 0$. On the other hand, a nonzero tilt angle β (assuming $\alpha = 0$) produces an antisymmetric profile consisting of two very similar features with opposite polarities. The change of the sign of either α or β leads to flipping the polarity of the corresponding $G(\theta)$ curve.

The theoretical model outlined above allows us to reproduce all transmission line shapes obtained experimentally under various combinations of tilt and rotation angles α and β . Note that in the plots of Fig. 3 the values of the rotation and tilt angles α and β are set equal to the corresponding experimental values and the resonance angles $\theta_{n,m}$ are computed using Eq. (8). The only free parameters are the normalization constant T_0 (adjusted for each plot) and the resonance width w_0 that is set equal to 6° for all resonances in all four plots.

As shown in Fig. 6, the SPP resonances $(\pm 1, \pm 1)^T$ localized at the metal-glass interface are also split by either tilt or rotation of the incidence plane, with RCP and LCP light coupling to different modes. However, the splitting is significantly smaller than that of the modes localized at the metal-air interface. More importantly, as shown in Fig. 4, these resonances are much more strongly broadened and have lower contrast due to the stronger damping of SPP waves in the Cr adhesion layer. We therefore do not expect these modes to produce a significant contribution to the CD signal. We have verified that including these modes in the calculation of the CD signal does not improve the agreement with the experimental data, unless their w_0 and T_0 parameters are tuned

separately. In order to keep the number of free parameters as low as possible, we exclude the $(\pm 1, \pm 1)^T$ modes from our analysis.

IV. CONCLUSIONS

In conventional analysis [8], chiroptic effects can be observed in a planar structure only when it lacks inversion symmetry. In that case, the system is characterized by three vectors: the wave vector of the incident light k_{Las} , the surface normal \hat{n} , and the direction along which the symmetry is broken. It is then possible to form a chiral arrangement of these vectors that will result in a circular dichroism and other chiroptic effects.

Nevertheless, our experimental data and SPP diffraction resonance modeling confirm the results of Ref. [11,13] and demonstrate that a symmetric square array of circular nanoholes could also exhibit chiroptic effects, such as circular dichroism. The apparent difference is resolved by taking into account the effect of spin-momentum locking of the propagating SPP waves [16,22]. Due to their transversal spin, the SPP waves are intrinsically chiral. A circularly polarized incident light couples only to the SPP wave of the same handedness. When the propagation direction (wave vector) of the SPP does not lie in the incidence plane, a chiral arrangement of k_{Las} , \hat{n} , and K_{SPP} is formed, leading to the circular dichroism, in agreement with Ref. [8].

Our work has established a connection between the observed circular dichroism effect and the spins of certain “diagonal” SPP modes of the nanohole array and their

propagation directions. Our model based on the transversal spin and spin-momentum locking of SPP waves provides a clear and simple qualitative explanation of the observed phenomena that successfully predicts the complicated angular dependence of the CD effect, as well as its dependence on the parameters of the nanohole array. These observations contribute to the existing picture of the EOT effect and the role played by spin-momentum locking and by the quantum spin Hall effect of light in EOT.

Plasmonic metasurfaces are known to produce dc photocurrents due to the photon drag or optical rectification effect, which is strongly amplified by the excitation of SPP resonances [22,27,28]. Combined with a purely electric readout based on the amplified optical rectification signal, our findings are suggestive of a mechanism available for orientation sensing with a smallest form factor in potential applications, for example, in flat thin-film gyroscopes and chiral molecule detection.

On the other hand, spin-momentum locking is not unique for SPP waves and plasmonic metasurfaces, and can be observed in other types of evanescent waves [16–18]. One may expect that the spin-momentum-locking mechanism and the induced dichroism reported here could even be better realized in nonplasmonic systems with the benefits of lower loss.

ACKNOWLEDGMENTS

This work was enabled by support from AFOSR, Grant No. FA9550-19-1-0355, and from ARO, Grants No. W911NF-14-2-0075 and No. W911NF-21-1-0181.

-
- [1] S. Du, Y. Wang, N. Alatrash, C. A. Weatherly, D. Roy, F. M. McDonnell, and D. W. Armstrong, *J. Pharm. Biomed. Analysis* **164**, 421 (2019).
 - [2] X. Wang and Z. Tang, *Small* **13**, 1601115 (2017).
 - [3] J. Kim, A. S. Rana, Y. Kim, I. Kim, T. Badloe, M. Zubair, M. Q. Mehmood, and J. Rho, *Sensors* **21**, 4381 (2021).
 - [4] A. V. Kondratov, M. V. Gorkunov, A. N. Darinskii, R. V. Gainutdinov, O. Y. Rogov, A. A. Ezhov, and V. V. Artemov, *Phys. Rev. B* **93**, 195418 (2016).
 - [5] X. Guo, C. Liu, and H. C. Ong, *Phys. Rev. Appl.* **15**, 024048 (2021).
 - [6] J. Lin, J. P. B. Mueller, Q. Wang, G. Yuan, N. Antoniou, X. C. Yuan, and F. Capasso, *Science* **340**, 331 (2013).
 - [7] B. Ai, H. M. Luong, and Y. Zhao, *Nanoscale* **12**, 2479 (2020).
 - [8] E. Plum, X. X. Liu, V. A. Fedotov, Y. Chen, D. P. Tsai, and N. I. Zheludev, *Phys. Rev. Lett.* **102**, 113902 (2009).
 - [9] T. Cao and M. J. Cryan, *J. Electr. Waves Appl.* **26**, 1275 (2012).
 - [10] E. Petronijevic, A. Belardini, G. Leahu, T. Cesca, C. Scian, G. Mattei, and C. Sibilia, *Appl. Sci.* **10**, 1316 (2020).
 - [11] B. M. Maoz, A. B. Moshe, D. Vestler, O. Bar-Elli, and G. Markovich, *Nano Lett.* **12**, 2357 (2012).
 - [12] O. Arteaga, B. M. Maoz, S. Nichols, G. Markovich, and B. Kahr, *Opt. Expr.* **22**, 13719 (2014).
 - [13] Z. L. Cao, L. Y. Yiu, Z. Q. Zhang, C. T. Chan, and H. C. Ong, *Phys. Rev. B* **95**, 155415 (2017).
 - [14] F. J. Garcia-Vidal, L. Martin-Moreno, T. W. Ebbesen, and L. Kuipers, *Rev. Mod. Phys.* **82**, 729 (2010).
 - [15] K. Y. Bliokh, A. Y. Bekshaev, and F. Nori, *Nat. Commun.* **5**, 3300 (2014).
 - [16] K. Y. Bliokh and F. Nori, *Phys. Rep.* **592**, 1 (2015).
 - [17] T. Van Mechelen and Z. Jacob, *Optica* **3**, 118 (2016).
 - [18] K. Y. Bliokh, D. Smirnova, and F. Nori, *Science* **348**, 1448 (2015).
 - [19] F. J. Rodriguez-Fortuno, G. Marino, P. Ginzburg, D. O’Connor, A. Martinez, G. A. Wurtz, and A. V. Zayats, *Science* **340**, 328 (2013).
 - [20] D. O’Connor, P. Ginzburg, F. J. Rodriguez-Fortuno, G. A. Wurtz, and A. V. Zayats, *Nat. Commun.* **5**, 5327 (2014).
 - [21] C. Liu, X. Y. Guo, and H. C. Ong, in *2018 Conference on Lasers and Electro-Optics (CLEO)* (Optical Society, Washington, 2018), p. JTh2A.48.
 - [22] P. Moroshkin, J. Plumitallo, T. Ochiai, R. Osgood, and J. M. Xu, *Phys. Rev. A* **106**, 023521 (2022).
 - [23] N. Shitrit, I. Yurevich, E. Maguid, D. Ozeri, D. Veksler, V. Kleiner, and E. Hasman, *Science* **340**, 724 (2013).
 - [24] Y. Gorodetski, A. Niv, V. Kleiner, and E. Hasman, *Phys. Rev. Lett.* **101**, 043903 (2008).
 - [25] J. Petersen, J. Volz, and A. Rauschenbeutel, *Science* **346**, 67 (2014).
 - [26] T. W. Ebbesen, H. J. Lezec, H. F. Ghaemi, T. Thio, and P. A. Wolff, *Nature (London)* **391**, 667 (1998).
 - [27] T. Hatano, T. Ishihara, S. G. Tikhodeev, and N. A. Gippius, *Phys. Rev. Lett.* **103**, 103906 (2009).
 - [28] M. Akbari, J. Gao, and X. Yang, *Appl. Phys. Lett.* **114**, 171102 (2019).